Control-Oriented Modeling and Layer-to-Layer Stability for Fused Deposition Modeling: A Kernel Basis Approach

Efe C. Balta, Dawn M. Tilbury, Kira Barton

***Abstract*— Additive manufacturing (AM) is an increasingly important enabler of smart manufacturing systems. Fused deposition modeling (FDM) is an AM technology that uses layer-wise extrusion to deposit material in 3D and most FDM machines run in open-loop. Due to the lack of feedback controllers, disturbances in the process cause failures. Although there are some spatial models for the FDM process, there are no layer-to-layer spatial dynamics models to enable control applications. This work proposes a novel modeling framework to capture the in-layer and layer-to-layer spatial dynamics of the FDM process utilizing a kernel basis approach. Individual kernels represent the deposition cross-sections and the orientation of the deposition. Layer-wise and layer-to-layer performance measures and stability definitions are proposed for the layer-to-layer spatial model. A simulation example is provided to demonstrate the validity of the stability criteria.**

I. Introduction and Background

Fused deposition modeling (FDM) is an additive manufacturing (AM) process in which a thermoplastic material is extruded through a heated nozzle in a numerically controlled deposition system. After a layer of material is deposited, the deposition system changes its height to accommodate the next deposition layer until all the layers of a 3D object are deposited. Some interesting applications of the FDM technology have been in advancing bone scaffold fabrication research [1], composite reinforced fabrication [2], and big area additive manufacturing [3].

FDM process dynamics shown in Fig. 1 can be separated into two groups. *Temporal dynamics*, such as heating the material [4], [5], volume flow through the nozzle [6] and the motion of the deposition system [7] are time dependent and constitute the transient response of the process. *Spatial dynamics*, such as the material volume and location in space, interactions with the build plate, and the geometry of the deposited beads and the printed part [8]–[10] constitute the spatial characteristics of the process.

A. Motivation and Problem Statement

A major concern with the FDM process is its reliability [11]. Poor reliability in FDM is caused by a lack of appropriate process models and feedback controllers, leading to significant cost and time losses [12]. Due to the lack of feedback controllers, disturbances in the printing process often result in severe errors in the printed part geometry. Since the current models do not capture the spatial dynamics of the process under disturbances, an FDM process may unexpectedly fail to manufacture the desired geometry or part functionality.

This work was funded in part by NSF #1544678.

Efe C. Balta, Dawn M. Tilbury, and Kira Barton are with the Department of Mechanical Engineering, University of Michigan, Ann Arbor, MI 48109, USA {baltaefe,tilbury,bartonkl}@umich.edu

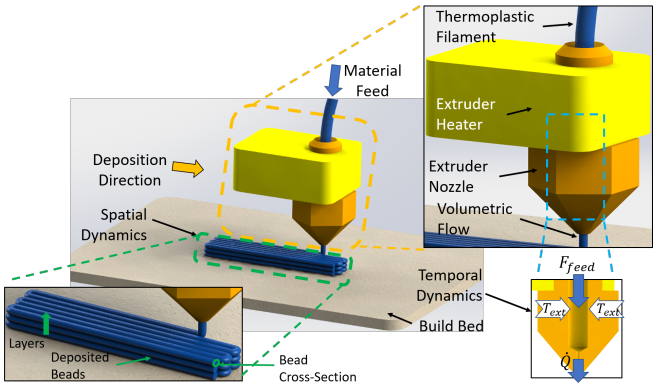

Fig. 1. Schematic of the FDM process. F_{feed} is the material feed force for the extrusion process in the nozzle. T_{ext} is the heat supplied by the extruder heater. $\dot{Q}$ is the volumetric flow through the nozzle.

Understanding the spatial dynamics of the individual layers and the relationship between layers will play a key role in understanding process stability over the layer domain and improving the reliability of the process. With the increasing use of Internet of Things (IoT) technologies in manufacturing, large amounts of process data are accessible [13]. Models that can capture the state of the process and enable predictions about the upcoming layers are needed to improve reliability. Therefore, FDM models that can capture the spatial dynamic states of the process at a given layer and determine layer-to-layer stability of the process should be developed. This work aims to address the reliability problem of the FDM, by developing a control-oriented layer-to-layer model to capture spatial dynamics of the process.

B. State-of-the-art in Spatial FDM modeling

An extensive review of the FDM modeling literature is given in [14]. A model for partial sintering between the deposited beads in FDM is proposed in [6], [15]. This model estimates the dimensionless neck growth between adjacent beads in transient and steady state conditions, but the spatial dynamics of the beads after sintering and the geometry of the beads are not given.

An ellipse cross-section model of the FDM process is proposed in [9]. The authors reported high accuracy with their model, but only modeled the surface roughness at the end of the process and not the layer-to-layer spatial dynamics. Hoelzle et al. proposed a circle with cut top and bottom as the deposited bead cross-section in a micro-robotic deposition process [16]. The authors used a computer vision

system to monitor the spatial distribution and the volume of the deposited material, but focused only on the temporal dynamics in their model development.

Comminal et al. proposed a computational fluid dynamics (CFD) model to estimate the bead cross-section geometry as a function of process parameters in FDM [17]. Their study compared various cross-section assumptions with their numerical analysis, but did not explore the layer-to-layer deposition aspect. Xia et al. proposed a novel numerical analysis framework to model the FDM process in [8]. This model captures the layer-to-layer spatial and temporal dynamics in a CFD framework. The proposed method is computationally expensive and not suitable for control applications. Cheng and Jafari considered process signatures that characterize surface defects through computer vision analysis, to model the spatial irregularities in the fused deposition of ceramics (FDC) process [18]. The model in [18] considered spatial errors and control actions for compensation. However, the model uses materials that spread into a rectangular cross-section upon deposition, and thermoplastics in an FDM process do not exhibit the same spreading behavior. Instead, most FDM materials retain their cross-sectional geometry after deposition.

In current literature, a method to derive a layer-to-layer spatial dynamics model for FDM does not exist. Therefore, this work aims to develop spatial dynamic models that can be used to analyze layer-to-layer stability of the deposition process. Three novel contributions of this work are: (1) a spatial in-layer model for FDM using kernel bases, (2) a spatial layer-to-layer dynamic model to understand spatial process dynamics and determine layer-to-layer stability, and (3) definitions of in-layer regularity and layer-to-layer stability for the proposed model. The remainder of the paper is structured as follows. Section II introduces the in-layer and layer-to-layer spatial dynamic models. Section III presents layer-to-layer stability measures. Section IV presents a simulation and case studies to demonstrate the proposed model. Concluding remarks and future directions are provided in Section V.

II. Proposed Modeling Approach

The modeling approach starts with a description of each layer as it is deposited and then describes how the layers build on each other.

A. In-Layer Deposition Model

In this model, we apply the bead geometry assumption proposed in [17] (Fig. 2). While this assumption may lead to oversimplifications in the geometry estimations under certain process parameters, it serves as a foundation for the kernel basis approach proposed in this paper. Extension to more complex geometries will be explored in later work.

1) Bead Cross-Section: Crockett and Calvert proposed the Hagen-Poiseuille flow for shear flow through the nozzle in the FDM process [19].

$$\dot{Q} = \frac{\pi R^4 \Delta P}{8 \nu L_t}, \tag{1}$$

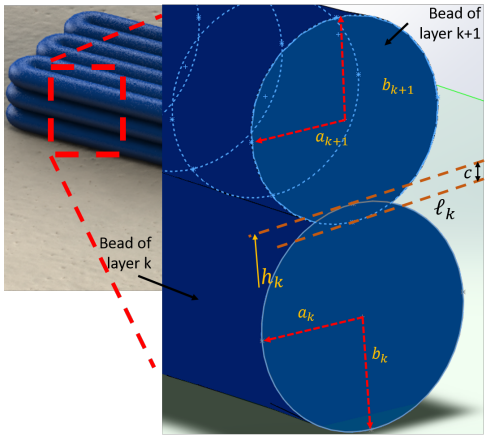

Fig. 2. Visualization of the ellipse bead model. The cross-sectional view of the bead is shown in the call-out. h_k is the height of the layer k (the total height up to layer k), c is the intersection between the subsequent layers, and ℓ is the hyperplane at which the bead of layer $k+1$ sits on.

where R is the nozzle size, L_t is the tip length of the nozzle, ΔP is the pressure drop in the extruder, which can be evaluated by similar work in [4], [16], ν is the viscosity of the extruded material, and $\dot{Q}$ is the volumetric flow rate. The cross-sectional area of the extruded bead shown in Fig. 2 is given as.

$$\dot{Q}/V_{ext} = \pi a b, \tag{2}$$

where, V_{ext} is the extruder speed, a is the radius of the ellipse aligning with the deposited layer plane denoting the width of the bead cross-section, and b is the radius of the ellipse along the height of the bead as shown in Fig. 2. This physical relationship captures the conservation of volume since the flow is assumed to be incompressible with no mass loss.

Assumption 1: Cross-sections of deposited beads in the FDM process can be approximated by ellipses with fixed aspect ratio $\alpha_r = b/a$, where a, b, are width and height radii of the ellipse.

Similar shape assumptions to Assumption 1 have been adopted in past work [6], [17]. Fixed aspect ratio used in this work is practical since the shape assumption is derived based on the conservation of volume in the extrusion process. Using Assumption 1, we rearrange Eq. (2) to have the height of the ellipse b as a function of the input pressure ΔP.

$$\Delta P \frac{R^4 \alpha_r}{8 \nu L_t V_{ext}} = b^2 \tag{3a}$$

$$u\,\psi = \sqrt{\Delta P}\,\psi = b, \quad \psi = \left(\frac{R^4 \alpha_r}{8 \nu L_t V_{ext}}\right)^{1/2} \tag{3b}$$

Denote u as the control input to the system, which is the square-root of the actual pressure at the extruder nozzle. ψ is a constant gain that relates the input u to the height b.

2) Spatial Layer Model: We define the global frame $F_A : (\hat{\boldsymbol{\imath}}_A, \hat{\boldsymbol{\jmath}}_A, \hat{\boldsymbol{k}}_A)$, where $(\hat{\boldsymbol{\imath}}_A, \hat{\boldsymbol{\jmath}}_A)$ are the in-layer deposition directions and $\hat{\boldsymbol{k}}_A$ is the deposition height direction. Let $\boldsymbol{v}(x_A, y_A) \in \mathbb{R}^2$ denote the in-layer deposition orientation at point $(x_A, y_A) \in F_A$. Then we define the local frame $F_P : (\hat{\boldsymbol{\imath}}_P, \hat{\boldsymbol{\jmath}}_P, \hat{\boldsymbol{k}}_P)$, where $\hat{\boldsymbol{\imath}}_P$ is aligned with $\boldsymbol{v}(x_A, y_A)$ and

$\hat{\boldsymbol{k}}_P$ is aligned with $\hat{\boldsymbol{k}}_A$. Therefore, F_P can be defined at any point in F_A, given $\boldsymbol{v}(x_A, y_A)$. Continuous deposition of a bead in a layer is represented as

$$S(x_A, y_A, z_A) = P(x_P, y_P) + C(a,b)|_{(\boldsymbol{v}(x_A,y_A))}, \quad (4)$$

where $S(x_A, y_A, z_A)$ is the bead geometry of the in-layer deposition, $P(x_P, y_P)$ is a deposition path, and $C(a,b)|_{(\boldsymbol{v}(x_A,y_A))}$ is the cross-sectional geometry of the bead at point (x_A, y_A). According to the ellipsoid assumption, we define the cross-section geometry as:

$$C(a,b)|_{\boldsymbol{v}(\bar{x}_A,\bar{y}_A)} \triangleq \frac{(y_A - \bar{y}_A)^2}{b^2} + \frac{(z_A - \bar{z}_A)^2}{a^2} \quad (5)$$

which defines the estimated ellipse cross-section at the spatial control point $(\bar{x}_A, \bar{y}_A)$.

In most AM processes such as selective laser sintering, jetting-based processes, direct metal deposition, and stereolithography there is a two dimensional (2D) spatial correlation between adjacently deposited materials in a layer. The spatial correlation is caused by coalescence of deposited material, which changes the deposited material geometry. In FDM, thermoplastic material does not spread upon extrusion and only partially sinters. The change of geometry due to partial sintering ($e.g.$ [6], [20]) between adjacent beads in a layer is negligible. Assumption 1 reduces the in-layer modeling problem to a one dimensional problem where the cross-sections of the ellipses along the deposition trajectory are to be determined.

B. Discretized Spatial Dynamics in Control Form

The model given in Eq. (4) is not in a control affine form. We want to model the spatial deposition height as the spatial state and the material input as the control input. It is convenient to represent the spatial state of the deposition process on a fixed discretized spatial field region. Spatial state (heightmap) based modeling for control of micro AM in which deposition directionality has no effect on the spatial state is presented in [21]. To capture the directional orientation of the deposited beads with their cross-sections, a kernel basis approach is presented here.

1) Kernel Basis for Directional Representation of Cross-Sections: For the discretized model, we will assume that all the in-layer (single layer) deposition is strictly on the spatial grid $L : (\mathbb{R}^{n_i} \times \mathbb{R}^{n_j})$ with its points discretized by $\Delta x = \Delta y = \gamma$. We will abuse the notation and use $L \in \mathbb{Z}^{n_i \times n_j}$ for the matrix representation of the spatial grid with L_{ij} as the element at the i^{th} row and j^{th} column, equivalently at coordinates (i, j).

Let $\mathbf{P}_k = [p_0^k, p_1^k, \ldots, p_{n_p^k}^k]$ denote the predefined deposition path of length n_p^k for layer k, where $p = [i, j]^T$ denotes the coordinates of the spatial control point on the grid and superscript T is a matrix transpose. Since the path length may vary between layers, we define $\eta = \eta_i \eta_j$ as the size of the bounding box for the deposition points throughout all layers, where η_i and η_j are the edge lengths of the bounding box. Therefore we have, $n_i = \eta_i + 2$ and $n_j = \eta_j + 2$. Let $\mathbf{I}_d \in \mathbb{R}^{\eta \times \eta}$ be a difference operator for $\mathbf{P}$, defined as

$$\mathbf{I}_d = \begin{bmatrix} -I & I & 0 & \ldots & 0 \\ 0 & -I & I & \ldots & 0 \\ \vdots & & \ddots & \ddots & \vdots \\ 0 & \ldots & 0 & -I & I \\ 0 & \ldots & 0 & -I & I \end{bmatrix}$$

where $I \in \mathbb{R}^2$ is the identity matrix. We evaluate $\mathbf{D} = \mathbf{I}_d vec(\mathbf{P})$, where $vec(\cdot)$ is the vectorization operator, as the vector representation of the directions $\mathbf{D} \in \mathbb{R}^{2\eta \times 1}$ between the consecutive spatial control points ($i.e.$ $d_m = p_{m+1} - p_m,\ d_m \in \mathbf{D}$). These directions are unit directions such that $d_m \in \mathbf{E}^2$, where $\mathbf{E}^2 = \{[\pm 1, \pm 1]^T, [\pm 1, 0]^T, [0, \pm 1]^T\}$.

The orientation of deposition at the spatial control point p and the geometry of the ellipse at the deposition point p with its neighboring points is represented with the kernel basis $K_p \in \mathbb{R}^{n_i \times n_j}$. K_p encodes information about the geometry deposited cross-section (Eq. (5)) and the orientation of the deposited bead ($\boldsymbol{v}(x_A, y_A)$). The single layer spatial deposition is represented as

$$\mathbf{S} = \sum_{m=0}^{\eta} K_{p_m} u_m, \quad (6)$$

where u_i is the input defined in Eq. (3b). For the layers with $\eta_k < \eta$, we have $K_{p_m} = u_m = 0$ for $m > \eta_k$. We can rewrite Eq. (6) equivalently in matrix form as:

$$\mathbf{S}_k = \mathbf{K}_k \mathbf{U}_k \quad (7a)$$

$$\mathbf{K}_k = [vec(K_{p_0}), vec(K_{p_1}), \ldots, vec(K_{p_\eta})]_k \quad (7b)$$

$$\mathbf{U}_k = [u_0, u_1, \ldots, u_\eta]_k^T, \quad (7c)$$

where, $\mathbf{S} \in \mathbb{R}^{n_i n_j}$, k is the layer index, $\mathbf{K} \in \mathbb{R}^{n_i n_j \times \eta}$, and $\mathbf{U} \in \mathbb{R}^{\eta}$. This matrix representation gives us a compact spatial form for the in-layer deposition model with the appropriate kernels. For the remainder of the paper, we will use the following convention for K matrices. K Matrices with tilde and standard font ($e.g.$ $\tilde{K}_i, \underline{\tilde{K}}$) denote kernel matrices of dimension 3×3, corresponding K matrices without tilde ($e.g.$ $K_i, \underline{K}_i$) denote the kernel basis matrices of full dimension $n_i \times n_j$, and the boldface matrices ($e.g.$ $\mathbf{K}_k, \underline{\mathbf{K}}_k, \bar{\mathbf{K}}_i$) are matrices comprised of individual kernel basis matrices for layer k. $\mathbf{K}_k$ denotes input kernel, $\underline{\mathbf{K}}_k$ denotes a kernel identifier associated with output states g_k, and $\bar{\mathbf{K}}_i$ denotes a matrix for identifying the height distribution as a function of spatial position.

2) Computation of Kernel Basis Matrices: The deposition model in Eq. (4) has the deposition direction ($P(x_P, y_P)$) and the cross-section at a given point ($C(a,b)|_{\boldsymbol{v}(\bar{x}_A,\bar{y}_A)}$). Based on the discretization L, the height of the deposited cross-section at spatial location L_{ij} is evaluated using Eq. (5). Since the deposition is on a grid point, the height of the bead cross-section at a neighboring grid point is:

$$z(\Delta y) = \sqrt{b^2 \left(1 - \frac{(\Delta y)^2}{a^2}\right)} + b \quad (8a)$$

$$\phi(b) = \psi z(\Delta y)/2b \quad (8b)$$

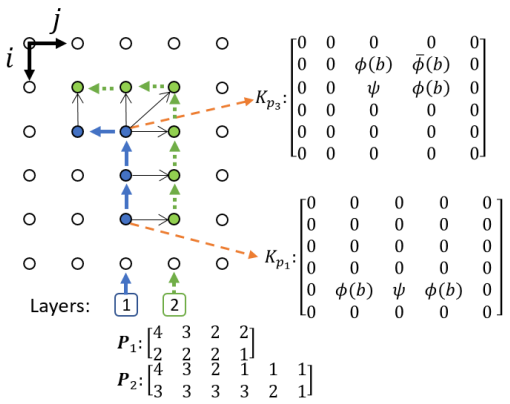

Fig. 3. Proposed kernel basis approach to represent the deposition process. The spatial grid $L \in \mathbb{Z}^{6\times5}$, with $\eta = 12$ is shown on left. Blue and green filled circles and corresponding solid and dashed arrows show the deposition coordinates for the first and second layers, respectively. $\mathbf{P}_1$ and $\mathbf{P}_2$ are the deposition points for the two layers respectively. Two kernels (K_{p_1}, K_{p_3}) from the first layer of the process are shown. Thin solid black arrows show the adjacency of the deposition points between two layers, which is represented by $\mathcal{A}_{(2|1)}$.

We will further constrain the control as $u \in [u_{\min}, u_{\max}]$; such that for a deposition at L_{ij}, the effect of the cross-section width is only observed on the neighboring points $L_{ij} + \zeta$, where $\zeta \in E^2$. An example deposition process is shown in Fig. 3. Therefore, we will define kernel matrices of size $\tilde{K}_m \in \mathbb{R}^{3\times3}$. Note that kernel matrices of different sizes can be developed for various deposition materials and length scales of interest. Depending on the orientation of the deposition at a spatial control point, the ellipse height profile of the bead cross-section can be represented by the following kernel matrices.

$$\tilde{K}_1 = \begin{bmatrix} 0 & 0 & 0 \\ \phi(b) & \psi & \phi(b) \\ 0 & 0 & 0 \end{bmatrix}, \quad \tilde{K}_2 = \tilde{K}_1^T = \begin{bmatrix} 0 & \phi(b) & 0 \\ 0 & \psi & 0 \\ 0 & \phi(b) & 0 \end{bmatrix}$$

Additionally, for the points where the direction changes we have the following kernel matrices, where $\bar{\phi}(b) = c_c\phi(b)$ denotes the height evolution at the corner points where the orientation changes (see Fig. 2). Due to the rapid change in the velocity vector, excessive deposition at sharp curvatures is reported in [22]. Constant $c_c \in (0, 1]$ is a model parameter to capture the excess deposition at corner points and can be adjusted for various FDM controllers. If there is no excess deposition, we evaluate $c_c = 0.29$ using the geometric relationship between the deposition points.

$$\tilde{K}_3 = \begin{bmatrix} \bar{\phi}(b) & \phi(b) & 0 \\ \phi(b) & \psi & 0 \\ 0 & 0 & 0 \end{bmatrix}, \tilde{K}_4 = \begin{bmatrix} 0 & \phi(b) & \bar{\phi}(b) \\ 0 & \psi & \phi(b) \\ 0 & 0 & 0 \end{bmatrix}$$

$$\tilde{K}_5 = \tilde{K}_4^{\,T}, \quad \tilde{K}_6 = \begin{bmatrix} 0 & 0 & 0 \\ 0 & \psi & \phi(b) \\ 0 & \phi(b) & \bar{\phi}(b) \end{bmatrix}$$

We define $\underline{\tilde{K}}$ for the spatial deposition path as

$$\underline{\tilde{K}} = \begin{bmatrix} 0 & 0 & 0 \\ 0 & 1 & 0 \\ 0 & 0 & 0 \end{bmatrix}.$$

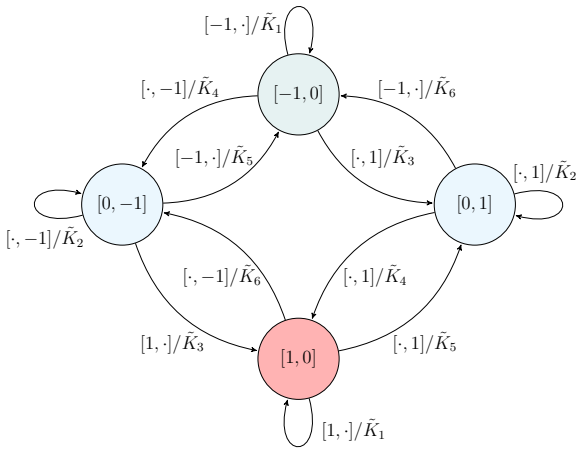

Fig. 4. Mealy automaton M for the evaluation of the basis kernels. $([\cdot,\cdot]/\tilde{K}_i)$ on each edge denote an input $d_m = [\cdot,\cdot]$ and an output $\tilde{K}_i \in \Lambda$ corresponding to the state and the input.

Each kernel $\tilde{K}_i$ is related to the unit directions in $\mathbf{E}^2$. Determining appropriate kernels for a set of deposition points depends on the knowledge of current and previous unit directions for the deposition point. We present a finite state machine to algorithmically evaluate the appropriate kernels for a deposition path $\mathbf{P}_k$. Consider the Mealy automaton $M = (Z, z_0, \Sigma, \Lambda, Tr, G)$, where Z denotes the deposition direction as states, z_0 is the initial state, Σ is a set of inputs, Λ is the set of outputs, $Tr : Z \times \Sigma \to Z$ is a transition function, $G : Z \times \Sigma \to \Lambda$ is an output function mapping the input and the state to the corresponding output. Automaton M is illustrated in Fig. 4. The vectors $d_m \in D$ are inputs to this automaton, $\Lambda = \{\tilde{K}_1, \dots \tilde{K}_6\}$ are the outputs, and G maps each d_m and state pair to one of the kernels in Λ. For example, appropriate kernels for the deposition path $\mathbf{P}_1$ in Fig. 3 is evaluated by $M_1 = (Z, [-1, 0], \Sigma_1, \Lambda_1, Tr, G)$, with $\Sigma_1 = \{[-1, 0], [-1, 0], [0, -1], [0, -1]\}$. The output string is $\Lambda_1 = \{\tilde{K}_1, \tilde{K}_1, \tilde{K}_4, \tilde{K}_2\}$, which denotes appropriate kernels for the deposition points in $\mathbf{P}_1$. Therefore, the automaton M is used for determining the appropriate kernels for the deposition points in each layer. After determining appropriate kernels, the kernel basis for each deposition point is evaluated. To evaluate a kernel basis K_m with kernel $\tilde{K}_m$ at location L_{ij}, we pad $\tilde{K}_m$ with zeros; $i-1$ above, n_i-i-1 below, $j-1$ to the left and n_j-j-1 to the right. The padding is done to have the kernel basis at the right spatial location L_{ij} and dimensionality (n_i, n_j).

3) Adjacency of layer-to-layer deposition points: To define the relationship between the spatial deposition points in subsequent layers, we define $\mathcal{A}_{(k|k-1)} \in \mathbb{R}^{\eta\times\eta}$ as the adjacency matrix of the η deposition points from layer $k-1$ to layer k. As shown in Fig. 3, with the change in number of path points between layers, we need to identify the deposition points in layer $k-1$ that will affect the height of the deposition points in layer k. Each row in $\mathcal{A}_{(k|k-1)}$ encodes the adjacency between two deposition points. If the height of the deposition point $p_1 = [i_1, j_1]^T$ in layer $k-1$ affects the height of the deposition point $p_2 = [i_2, j_2]^T$ in layer k, we have $\mathcal{A}_{(k|k-1)}(j_2\eta_j + i_2, j_1\eta_j + i_1) = 1$.

C. State-space Representation of Layer to Layer Dynamics

The state-space representation is an extension of the previous work in [10], for the FDM process. The FDM layer-to-layer dynamics over a spatial field of interest L can be represented as

$$g_{k+1} = H_k^g g_k + H_k^u \mathbf{U}_k + H_k^c \boldsymbol{c} \tag{9}$$

where $g_k \in \mathbb{R}^{n_i n_j \times 1}$ represents the spatial state of the process at layer k. Spatial state for the deposition process is the height of the deposition at each coordinate $(i,j) \in L$. $H_k^g \in \mathbb{R}^{n_i n_j \times n_i n_j}$ is a matrix that captures the effect of the previous layer's state on the subsequent layer, $\mathbf{U}_k$ is the input for layer k (Eq. (7c)), $H_k^u \in \mathbb{R}^{n_i n_j \times \eta}$ is the spatial input matrix that captures the spatial dynamics of the in-layer deposition, and $H_k^c \in \mathbb{R}^{n_i n_j \times \eta}$ is the matrix that captures the effect of bead intersection between successive layers.

To investigate the effect of the previous layer on subsequent layers, it is important to recognize that deposited beads of successive layers intersect each other at their interfaces [9], [20]. As shown in Fig. 2, beads in different layers $(k, k+1)$ intersect, such that the bottom of the bead of layer $k+1$ is below the top of the bead of layer k. We denote the height of intersection between layers with $c \in \mathbb{R}$ (shown in Fig. 2), and have $\boldsymbol{c} = c\mathbf{1}^{\eta \times 1}$. To model the height evolution between the layers, we determine the height of the hyperplane ℓ between successive layers. Fig. 2 shows two successive layers, the hyperplane ℓ and the height of intersection c, where h_k denotes the height of the cross-sections at the spatial deposition point. Height of the hyperplane ℓ for layer k is defined as $\ell_k = h_k - c$.

Similar to Eq. (7), we define the kernel identifier associated with the spatial state at layer k as

$$\underline{\mathbf{K}}_k = [vec(\underline{K}_{p_0}), vec(\underline{K}_{p_1}), \ldots, vec(\underline{K}_{p_\eta})]_k^T \tag{10}$$

where $\underline{K}_{p_m}$ is the kernel basis evaluated by the kernel $\underline{\tilde{K}}$ at location p_m. Additionally, we define the matrix $\bar{\mathbf{K}}_k$ as

$$[\bar{\mathbf{K}}_k]_{mn} = \begin{cases} c_r / n_z([\mathbf{K}_k]_m), & if \quad n_z([\mathbf{K}_k]_m) > 1, \\ 1, & if \quad n_z([\mathbf{K}_k]_m) = 1, \\ 0, & otherwise \end{cases} \tag{11}$$

where, $n_z([\mathbf{K}_k]_m)$ is the number of non-zero entries of the m^{th} row of $\mathbf{K}_k$ (Eq. (7b)), and $c_r \in (0,1]$ is a design parameter to capture material deposition at the corners. The parameter c_r represents the height evolution at the inner curvature of the corner. Choosing $c_r = 1$ yields a height equal to the average of heights $\phi(b)$ of the contributing kernels at the corner. We also define the matrix $\delta\mathbf{K}_k \in \mathbb{R}^{n_i n_j \times n_i n_j}$ to consistently capture the height evolution of the spatial points in layer k that have no deposition on them in the subsequent layer.

$$\delta\mathbf{K}_k = \mathbf{diag}(q_i), \; q_i = \begin{cases} 1, & if \quad [\boldsymbol{S}_k]_i = 0, \\ 0, & otherwise. \end{cases} \tag{12}$$

Then, we construct the state matrix H_k^g as follows.

$$H_k^g = \bar{\mathbf{K}}_k \mathcal{A}_{(k|k-1)} \underline{\mathbf{K}}_{k-1} + \delta\mathbf{K}_k. \tag{13}$$

H_k^g is an operator on g_k, such that $\bar{\mathbf{K}}_k \mathcal{A}_{(k|k-1)} \underline{\mathbf{K}}_{k-1} g_k$ gives the height h_k at the deposition points from the previous layer and $\delta\mathbf{K}_k g_k$ gives the height of the points that have no deposition at layer k. By knowing h_k at layer k, we evaluate the height of the plane ℓ_k at each spatial point, using the operator H_k^c and add the input $\mathbf{U}_k$ for the next layer using the operator H_k^u. H_k^u and H_k^c for layer k are defined as

$$H_k^u = \mathbf{K}_k, \quad H_k^c = -\bar{\mathbf{K}}_k. \tag{14}$$

Since the deposition path is predefined for each layer in the FDM process, matrices H_k^g, H_k^u, H_k^c can be pre-calculated for each layer.

III. Layer-to-layer stability

Here we develop the tools to analyze the layer-to-layer stability of the layer-to-layer spatial dynamic process given in Eq. (9).

A. Layer-wise Regularity

Let $g_k^d \in \mathbb{R}^{n_i n_j \times 1}$ denote the desired layer profile at layer k and $\omega \in \mathbb{R}$ denote the admissible deviation from the desired profile such that we have $\underline{\omega}_k = \left\|g_k^d\right\|_2 - \omega$ and $\bar{\omega}_k = \left\|g_k^d\right\|_2 + \omega$ as design limits. Following regularity definition is proposed for the development of layer-to-layer stability.

Definition 1: A process is layer-wise regular in layers $(k_0, k_0+n]$ if $\left\|g_k^d - g_k\right\| \leq \omega$ for all $k \in (k_0, k_0+n]$.

B. Layer-to-layer Stability

We introduce $\tilde{g}_k = T_k(I - \boldsymbol{S}_k) g_k$ as the heights of spatial points that had deposition on them in layer k. The elements of $\tilde{g}_k$ are the heights of deposition points up to layer k and $T_k : \mathbb{R}^{n_i n_j} \to \mathbb{R}^{\bar{n}_k}$ is a uniform projection, where $\bar{n}_k = n_z(\boldsymbol{S}_k)$. Then we have $\tilde{g}_k \succ 0$. Let $\min_j(\|\tilde{g}_k(j)\|_1)$ denote the element-wise L_1-norm minimum of vector $\tilde{g}_k$. The process in Eq. (9) has a bounded input ($i.e.$ deposition input) and spatial state g_k is always bounded from above. Additionally, we assume the layer height input (for a single layer) is identical throughout the layers in the process.

Definition 2: A layer-wise spatially varying deposition process of the form in Eq. (9) bounded from above as $\|g_k\|_\infty < \Phi_k$ for some constant $\Phi_k > 0$ is said to be:

(i) Layer-to-layer geometrically stable (L2LGS) if $\|g_{k-1}\|_\infty \leq \min_j(\|\tilde{g}_k(j)\|_1)$ for all $k \in (1, n_\ell]$,

(ii) layer-to-layer stable if it is L2LGS and layer-wise regular for all $k \in (1, n_\ell]$,

An important remark is that the spatial state g_k denotes the height (top of ellipse cross-sections) of all the points in the spatial domain L at layer k. Then, L2LGS states that the minimum height of the spatial deposition points in layer k must have a height that is greater than the maximum height at the layer $k-1$. This geometric condition ensures that newly deposited material at layer k is adding to the height of the build and not falling onto the substrate or the prior layers. Layer-to-layer stability condition states that a part should be L2LGS and the height of individual layers should

be within the design tolerance bound (ω). Thus, layer-to-layer stability is as restrictive as the tightness of the design dimension tolerances.

Next we will introduce the main theorem to ensure the layer-to-layer geometric stability. Define $W_{k-1} = \bar{\mathbf{K}}_{k-1}\underline{\mathbf{K}}_{k-1}$ with the structure $W = [w^1, \ldots, w^{n_i n_j}]$, where w^i are the columns of W. Then $w^i \in span\{v^i\}$, where $\{v^i\}_1^{n_i n_j} \in \mathbb{R}^{n_i n_j}$ are the standard basis vectors for $\mathbb{R}^{n_i n_j}$. Let $\bar{V} = \{v^{i_0}, \ldots, v^{i_n}\}$ denote the set of basis vectors needed to construct the columns $w^i \in W_{k-1}$.

Theorem 1: The spatial dynamic process in Eq. 9 is L2LGS if and only if $\underline{\mathbf{K}}_k^T \in span(\bar{V})$, where $\bar{V}$ is the set of standard basis vectors in $\mathbb{R}^{n_i n_j}$ to construct the invariant transformation $W_{k-1} = \bar{\mathbf{K}}_{k-1}\underline{\mathbf{K}}_{k-1}$.

Theorem 1 states that in order to be L2LGS, a spatial input point p should have some fraction of a bead deposited below in the previous layer. In the current formulation, Theorem 1 dictates that there should be at least half a bead below a spatial input point for L2LGS condition to hold. This is a result of the fact that deposited material in layer k will fall onto the substrate or prior layers if there is no material present in layer $k-1$ to support the deposition in layer k.

A sketch of the proof for Theorem 1 is given as follows. Suppose a spatial point $v \in \underline{\mathbf{K}}_k^T$ has material deposition by $\mathbf{U}_k$. If we have $v \in \bar{V}$, it means that there has been material deposited at v from the previous layer, then the process in Eq. (9) is L2LGS. Going the other direction, suppose for an L2LGS process we have $v \in \underline{\mathbf{K}}_k^T$ and $v \notin \bar{V}$. Thus, no material is deposited at v in the previous layer but there is material deposited with $\mathbf{U}_k$, which results in a condition that contradicts with the definition of L2LGS since the newly deposited material is not adding up to the height of the build.

Remark 1: The fraction of sufficient bead support is based on the geometric assumptions in this work. Additional considerations for material properties and process parameters (speed, temperature) may be included in future work.

IV. Case Study

A simulation of an FDM process is implemented in MATLAB software. The spatial input for the simulation is shown in Fig. 5. The 15 layer input in Fig 5 is an inverted pyramid with successive layers moving outward and is L2LGS. The L2LGS condition is ensured by designing the deposition path according to Theorem 1 such that each deposition point is supported from below by material in the previous layer.

A. Setup

An example of an FDM process is experimentally demonstrated on an Ultimaker 3© printer with polylactic acid (PLA) filament and $0.2mm$ layer height. In this experimental demonstration, we consider three case studies: (1) L2LGS part, (2) L2L geometrically unstable part, and (3) L2L unstable part that satisfies L2LGS but violates the layer regularity condition. Process parameters for all three cases include: $\psi = 3.87\ [mm/Pa], \phi(b) = 0.5\psi, n_i = n_j = 25, \eta = 529, c_r = 0.98, c_c = 0.6, c = 0.05\ mm, \omega = 2$. Desired layer height is $h_d = 0.2mm$ and the identical deposition input is

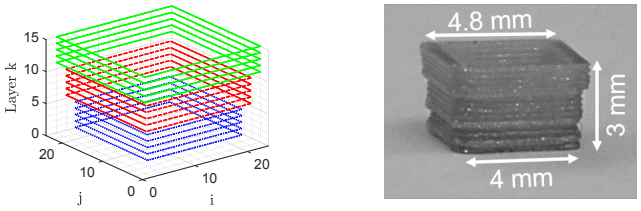

(a) (b)

Fig. 5. Illustration of deposition path for designed case study geometry. (a) Deposition starts at the first layer and moves up layer by layer. Bottom five layers shown with blue dotted lines, mid five layers shown with red dashed lines and the top five layers shown with green solid lines. (b) Image of the printed inverted pyramid geometry.

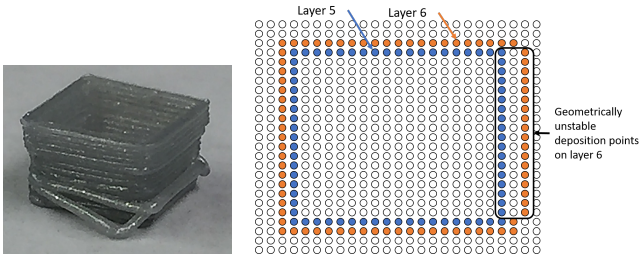

Fig. 6. (a) Illustration of the L2L geometric unstable process. Deposition is not supported by material from below, along an edge at layer 6. As a result, the deposited bead falls onto the substrate. (b) Filled circles show the deposition points for layer 5 and layer 6. Unsupported edge deposition points on layer 6 are shown in the black rectangle.

$u = h_d/\psi$ for spatial input points throughout layers. A zero-mean Gaussian process noise $\mathcal{N}(0, \sigma_g^2)$ with $\sigma_g = 0.25$, and $\alpha_r = 2/3$ is applied to the input in the simulation. Case (2) has been designed to violate L2LGS for demonstration purposes, while case (3) demonstrates a high model disturbance $\sigma_g = 1.75$ at layer 7. An unexpected disturbance may occur due to a power surge, a physical disturbance to the system or due to inconsistencies in the material. A classification of anomalies in manufacturing systems is given in [23] and will not be discussed in detail here. We assume that the disturbances in the process manifest themselves in height variation and no spatial deposition variation is observed.

B. Results and Discussion

1) Case 1 - Layer-to-layer Geometrically Stable: The deposition shown in Fig. 5 is designed such that it fits inside a slot with a tolerance ω. Since L2L stability implies that the layers will be within the ω bound, stable parts will fit inside the slot whereas L2L unstable parts, although being structurally sound, will not have the desired dimensions and would fail to fit inside the slot. For this experimental study, $\alpha_r = 0.5$. First five layers have 72 deposition points, second five layers have 80 deposition points and last five layers have 88 deposition points (see Fig. 5).

2) Case 2 - Layer-to-layer Geometrically Unstable: Fig. 6 shows a layer-to-layer geometrically unstable process. The deposition path at layer 6 is modified to violate the condition given in Theorem 1. Half of the deposition points along an edge at layer 6 are moved so that the moved deposition points do not have any overlap with the previous layer bead along

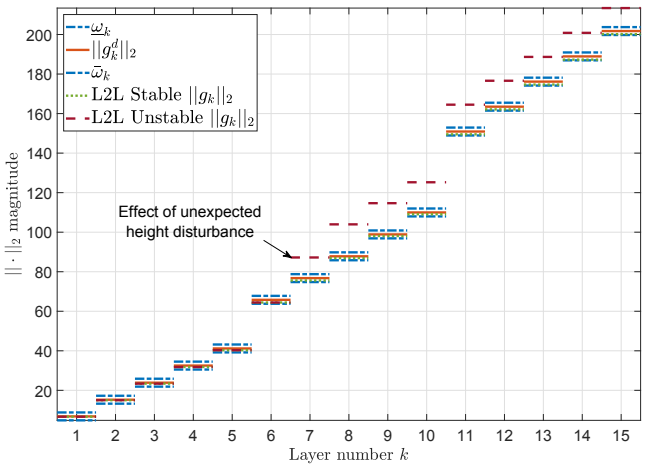

Fig. 7. Illustration of the L2L unstable deposition process, caused by the disturbance on layer 7. This condition continues for the remaining deposition layers, resulting in a part that fails to meet the design requirements.

that edge (see Fig. 6 (b)). This change has been implemented in the G-Code that runs the FDM printer. As a result, the deposited bead at unsupported deposition points falls onto the substrate during the deposition process.

3) Case 3 - Layer-to-layer Unstable: The L_2-norm of the spatial states of the deposition process, desired state norms and the tolerance limits are shown on the graph in Fig. 7. An L2L stable process has state norms within the bounds over all layers. A disturbance during the 7th iteration pushed the height outside of the layer-wise regularity condition, thus rendering the part L2L unstable. This condition continues for the remaining deposition layers, resulting in a part that fails to meet the design requirements. After the L2L unstable condition is detected at layer 7, the deposition may be stopped to save time and material.

V. Conclusion

Additive manufacturing is a key enabler of smart manufacturing, but the poor reliability of AM processes hinders their utility in practical applications [24]. This work proposes a novel spatial modeling approach to develop control-oriented models for the fused deposition modeling process. A kernel basis approach is proposed for capturing the cross-sectional geometry of the deposited beads along with directionality. Layer-wise regularity and layer-to-layer stability measures are defined with the proposed model. These definitions play an important role in assessing the geometric and spatial stability of the FDM processes, which has not been proposed before. The proposed modeling framework is demonstrated through experimental and simulation case studies. Future work will focus on model validation and controller design to modify an L2L unstable process.

References

[1] I. Zein, D. W. Hutmacher, K. C. Tan, and S. H. Teoh, "Fused deposition modeling of novel scaffold architectures for tissue engineering applications," *Biomaterials*, vol. 23, no. 4, pp. 1169–1185, 2002.

[2] B. Brenken, E. Barocio, A. Favaloro, V. Kunc, and R. B. Pipes, "Fused filament fabrication of fiber-reinforced polymers: A review," *Additive Manufacturing*, 2018.

[3] C. E. Duty, V. Kunc, B. Compton, B. Post, D. Erdman, R. Smith, R. Lind, P. Lloyd, and L. Love, "Structure and mechanical behavior of big area additive manufacturing (BAAM) materials," *Rapid Prototyping Journal*, vol. 23, no. 1, pp. 181–189, 2017.

[4] A. Bellini, S. Guceri, and M. Bertoldi, "Liquefier Dynamics in Fused Deposition," *Journal of Manufacturing Science and Engineering*, vol. 126, no. 2, p. 237, 2004.

[5] M. A. Yardimci and G. Selçuk, "Conceptual framework for the thermal process modelling of fused deposition," *Rapid Prototyping Journal*, vol. 2, no. 2, pp. 26–31, 1996.

[6] C. Bellehumeur and L. Li, "Modeling of bond formation between polymer filaments in the fused deposition modeling process," *Journal of Manufacturing Processes*, vol. 6, no. 2, pp. 170–178, 2004.

[7] S. Bukkapatnam and B. Clark, "Dynamic modeling and monitoring of contour craftingan extrusion-based layered manufacturing process," *Journal of Manufacturing Science and Engineering*, vol. 129, no. 1, p. 135, 2007.

[8] H. Xia, J. Lu, S. Dabiri, and G. Tryggvason, "Fully resolved numerical simulations of fused deposition modeling. Part I: fluid flow," *Rapid Prototyping Journal*, vol. 24, no. 2, pp. 463–476, 2018.

[9] D. Ahn, J. H. Kweon, S. Kwon, J. Song, and S. Lee, "Representation of surface roughness in fused deposition modeling," *Journal of Materials Processing Technology*, vol. 209, no. 15-16, pp. 5593–5600, 2009.

[10] D. J. Hoelzle and K. L. Barton, "On spatial iterative learning control via 2-D convolution: Stability analysis and computational efficiency," *IEEE Transactions on Control Systems Technology*, vol. 24, no. 4, pp. 1504–1512, 2016.

[11] E. C. Balta, D. M. Tilbury, and K. Barton, "A centralized framework for system-level control and management of additive manufacturing fleets," in *Automation Science and Engineering (CASE), 2018 14th IEEE Conference on*. IEEE, 2018.

[12] J. Pellegrino, T. Makila, S. Mcqueen, and E. Taylor, "Measurement science roadmap for polymer-based additive manufacturing," *NIST Adv. Manuf. Ser*, vol. 100, 2016.

[13] K. Barton, F. Maturana, and D. Tilbury, "Closing the loop in IoT-enabled manufacturing systems: Challenges and opportunities," in *2018 Annual American Control Conference (ACC)*. IEEE, 2018, pp. 5503–5509.

[14] B. N. Turner, R. Strong, and S. A. Gold, "A review of melt extrusion additive manufacturing processes: I. Process design and modeling," *Rapid Prototyping Journal*, vol. 20, no. 3, pp. 192–204, 2014.

[15] Q. Sun, G. Rizvi, C. Bellehumeur, and P. Gu, "Effect of processing conditions on the bonding quality of FDM polymer filaments," *Rapid Prototyping Journal*, vol. 14, no. 2, pp. 72–80, 2008.

[16] D. J. Hoelzle, A. G. Alleyne, and A. J. W. Johnson, "Iterative learning control for robotic deposition using machine vision," *2008 American Control Conference*, pp. 4541–4547, 2008.

[17] R. Comminal, M. P. Serdeczny, D. B. Pedersen, and J. Spangenberg, "Numerical modeling of the strand deposition flow in extrusion-based additive manufacturing," *Additive Manufacturing*, vol. 20, pp. 68–76, 2018.

[18] Y. Cheng and M. A. Jafari, "Vision-based online process control in manufacturing applications," *IEEE Transactions on Automation Science and Engineering*, vol. 5, no. 1, pp. 140–153, 2008.

[19] R. S. Crockett and P. D. Calvert, "The liquid-to-solid transition in stereodeposition techniques," *1996 Solid Freeform Fabrication (SFF) Proceedings*, pp. 257–264, 1996.

[20] S. Ahn, M. Montero, D. Odell, S. Roundy, and P. K. Wright, "Anisotropic material properties of fused deposition modeling ABS," *Rapid Prototyping Journal*, vol. 8, no. 4, pp. 248–257, 2002.

[21] C. Pannier, M. Wu, D. Hoelzle, and K. Barton, "LPV models for jet-printed heightmap control," *2019 American Control Conference*, 2019.

[22] D. S. Ertay, A. Yuen, and Y. Altintas, "Synchronized material deposition rate control with path velocity on fused filament fabrication machines," *Additive Manufacturing*, vol. 19, pp. 205–213, 2018.

[23] F. Lopez, M. Saez, Y. Shao, E. C. Balta, J. Moyne, Z. M. Mao, K. Barton, and D. Tilbury, "Categorization of anomalies in smart manufacturing systems to support the selection of detection mechanisms," *IEEE Robotics and Automation Letters*, vol. 2, no. 4, pp. 1885–1892, 2017.

[24] E. C. Balta, Y. Lin, K. Barton, D. M. Tilbury, and Z. M. Mao, "Production as a service: A digital manufacturing framework for optimizing utilization," *IEEE Transactions on Automation Science and Engineering*, vol. 15, no. 4, pp. 1483–1493, Oct 2018.